

# Effect of Inversion Asymmetry on Bilayer Graphene's Superconducting and Exciton Condensates

Xiang Hu,<sup>1</sup> Enrico Rossi,<sup>2</sup> and Yafis Barlas<sup>3</sup>

<sup>1</sup>*School of Physical Science and Technology, Guangxi Normal University, Guilin 541004, China*

<sup>2</sup>*Department of Physics, William & Mary, Williamsburg, VA, 23187.*

<sup>3</sup>*Department of Physics, University of Nevada, Reno, NV, 89557.*

(Dated: April 12, 2023)

Inversion asymmetry in bilayer graphene can be tuned by the displacement field. As a result, the band dispersion in biased bilayer graphene acquires flat band regions near the Dirac points along with a non-trivial band geometry. We analyze the effect of inversion symmetry on the critical temperature and superfluid stiffness of the superconducting state of AB-stacked graphene bilayer and on the exciton condensate in double layers formed by two AB-stacked graphene bilayers. The geometric superfluid stiffness in bilayer graphene superconductors is found to be negligible due to the small superconducting gap. Furthermore, we show that the geometric superfluid stiffness is maximized for a constant order parameter. Therefore, it can be neglected in biased bilayer graphene superconductors with any pairing symmetry. However, the displacement field enhances the geometric superfluid stiffness in exciton condensates. It is most prominent at low densities and high displacement fields. A consequence of the geometric superfluid stiffness is a modest enhancement of the Berezinskii-Kosterlitz-Thouless transition temperature in bilayer graphene's exciton condensate.

## I. INTRODUCTION

The recent discovery of superconductivity [1–7] and correlated phases [8–13] in twisted two-dimensional crystals [14] has brought attention to the role of non-trivial band geometry in multi-orbital superconductors [15–24] and other strongly correlated states. [13, 25–35] Non-trivial band geometry in multi-orbital superconductors [1–7] and exciton condensates results in a geometric superfluid stiffness associated with inter-band excitations of the condensate. For isolated bands, the inter-band contribution to the superfluid stiffness can be projected onto the lowest energy and is proportional to the quantum metric of the band. [16] In contrast, the conventional superfluid stiffness is proportional to the electron density and inversely proportional to the band's effective mass. [36] Consequently, the geometric superfluid weight dominates in flat band superconductors and exciton condensates [35, 37], such as superconducting twisted bilayer graphene [1–4] and twisted multi-layer graphene [5–7] at magic angles. Additionally, the quantum metric is lower-bounded by the absolute value of the Berry curvature. Therefore superconductors in the topological and Wannier obstructed bands [15, 18, 38–40] exhibit a finite superfluid stiffness. [41]

Until recently, the geometric superfluid weight has only been studied for flat or weakly dispersive isolated bands. However, situations arise where an otherwise dispersive band contains large flat regions in momentum space, as in multi-layer graphene systems. [42–47] Since pairing interactions are typically projected close to the Fermi energy if the Fermi energy also coincides with these flat regions, the geometric superfluid density can be comparable to its conventional counterpart. Additionally, to maximize the flat band regions and geometric superfluid density, it would be ideal to engineer situations where

the local extrema of the Berry curvature also coincide with such flat band regions. In bilayer graphene, the flat band regions appear at the Dirac points, in the vicinity of which the Berry curvature and the quantum metric exhibit maximum values. The tunability of the band structure and Berry curvature of biased bilayer graphene by displacement fields and control of total density in dual-gated samples make it possible to satisfy these stringent constraints.

In this work, we analyze the geometric and conventional superfluid stiffness ratio, which can be tuned by displacement fields in biased-bilayer graphene superconductors [48, 49] and exciton condensates. [50] We first perform a mean-field analysis of superconductivity and exciton condensation in dual-gated bilayer graphene in the presence of a mass term  $m$  due to broken  $\mathcal{C}_2$  symmetry. This mass term corresponds to the displacement field between the layers. We assume a momentum-independent order parameter at the Fermi surface in both cases. Inversion asymmetry, characterized by  $m$ , enhances the superconducting and excitonic gap, increasing the critical temperature  $T_c$ . We find that for small changes in mass term  $m \sim 0-40$  meV, the self-consistent value of the superconducting gap increases by several orders of magnitude. However, the associated  $T_c \sim 1-100$  mK is small. In contrast, the enhancement of the exciton gap is less pronounced but its  $T_c$  can be larger. This is due to the long-range nature of the pairing attraction in exciton condensates. The exciton gap is maximized for an optimal value of the density-dependent mass  $m(n)$  providing critical temperatures  $T_c \sim 1-10$ K. This provides a sweet spot to search for the elusive exciton condensate in double-bilayer graphene systems.

The superfluid density for the two cases exhibits very different behaviors. In the case of superconductors, while the geometric superfluid density enhancement follows the superconducting gap, it is negligible compared to the con-

ventional superfluid density. This is due to the small values of the superconducting gap. However, for the exciton condensate, the geometric contribution is of the same order as the conventional superfluid density. As a result, the geometric superfluid stiffness for the exciton condensate exhibits a rich phenomenology, the most striking of which is a density-dependent maximum value as a function of the mass term  $m$ . We analyze the Berezinskii-Kosterlitz-Thouless (BKT) transition temperature ( $T_{\text{BKT}}$ ) for the exciton condensate. [51] The additional geometric superfluid density increases  $T_{\text{BKT}}/T_c$ , which is more pronounced at low densities and large values of  $m$ .

The paper is organized as follows: Section I reviews chiral two-dimensional electron systems' geometric and topological properties. In section II, we solve the self-consistent gap equation for the superconductor, and the exciton condensates as a function of the density  $n$  and the mass  $m$ . In section III, we calculate the superfluid density and discuss the enhancement of the geometric superfluid stiffness for both cases. Finally, section IV discusses the influence of the mass term on the BKT transition in exciton condensates. We conclude by discussing the relevance of our results to experiments in superconducting and exciton condensates in biased bilayer graphene.

## II. CHIRAL 2DEGS: GEOMETRIC PROPERTIES

The electronic properties of single and multi-layer graphene 2D crystals are described by the chiral two-dimensional electron gas (C2DEG) Hamiltonian. This class of  $\mathbf{k} \cdot \mathbf{p}$  Hamiltonians is defined for the electron envelope wavefunction momenta  $\mathbf{k}$  near the Dirac points  $K(K')$  denoted by  $\eta = \pm$ . The chiral 2DEG Hamiltonian:  $\mathcal{H}_{0,\eta} = \sum_{\mathbf{k},\eta} \mathbf{c}_{\mathbf{k},\eta}^\dagger \hat{\mathcal{H}}_{0,\eta} \mathbf{c}_{\mathbf{k},\eta}$  with chirality index  $J$ ,

$$\hat{\mathcal{H}}_{0,\eta} = \zeta_J k^J \left( \cos(J\varphi_{\mathbf{k}}) \hat{\sigma}_x + \eta \sin(J\varphi_{\mathbf{k}}) \hat{\sigma}_y \right) + m \hat{\sigma}_z, \quad (1)$$

captures a chirality-dependent electronic dispersion. In Eq. (1),  $\hat{\sigma}_i$  correspond to the Pauli matrices defined in the sublattice space, while the momenta,  $k = (k_x^2 + k_y^2)^{1/2}$  with  $\varphi_{\mathbf{k}} = \tan^{-1}(k_y/k_x)$  and  $\zeta_J$  denotes a constant in units of eV/nm $^J$ ,  $\zeta_1 = \hbar v$  for graphene and  $\zeta_2 = (\hbar v)^2/\gamma_1$  ( $\gamma_1 \sim 0.4$  eV) for bilayer graphene systems, with  $v \approx 1 \times 10^6$  m/s. The Hamiltonian acts on the two-component spinor  $\mathbf{c}_{\mathbf{k},\eta}^\dagger = (c_{\mathbf{k},A,\eta}^\dagger, c_{\mathbf{k},B,\eta}^\dagger)$ , with  $c_{\mathbf{k},A(B),\eta}^\dagger (c_{\mathbf{k},A(B),\eta})$  denoting the creation (annihilation) fermionic operator for a given sub-lattice  $A(B)$  in the  $\eta$  valley.

The mass term  $m$  breaks  $\mathcal{C}_2$  symmetry, however, the system still retains particle-hole and time-reversal symmetry, expressed as  $\sigma_y \hat{\mathcal{H}}_{0,\eta} \sigma_y = -\hat{\mathcal{H}}_{0,-\eta}^T$  and  $\hat{\mathcal{H}}_{0,\eta} = \hat{\mathcal{H}}_{0,-\eta}^T$  respectively. The energy dispersion for the inversion asymmetric chiral 2DEG is  $\epsilon_{\mathbf{k},J} = \pm(\zeta_J^2 k^{2J} + m^2)^{1/2}$ . For biased-bilayer graphene,  $J = 2$  the density of states

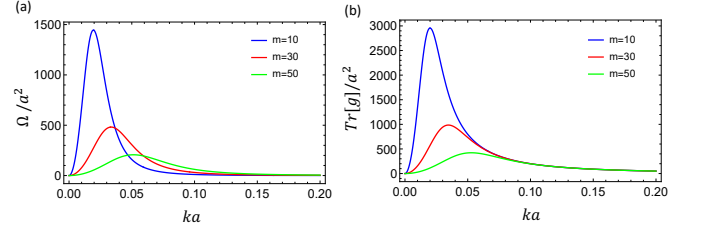


FIG. 1. a) Berry curvature  $\Omega(\mathbf{k})$  and b) trace of the  $g_{\mu\nu}(\mathbf{k})$  in units of  $a^2$  as a function of  $ka$  for different values of the displacement field,  $a \sim 0.246$  nm is graphene's lattice constant.

is enhanced for  $\epsilon \approx m$ ,

$$D_{J=2}(\epsilon) = \frac{N(0)}{\sqrt{\epsilon^2 - m^2}} \Theta(\epsilon^2 - m^2), \quad (2)$$

where  $N(0) = \gamma_1/(4\pi(\hbar v)^2)$  and  $\Theta$  is the Heaviside function. This divergent behavior at  $\epsilon \approx m$  is critical for the superconducting and exciton gap in biased-bilayer graphene, as discussed in the next section.

The quantum geometry of a band can be described by a gauge-invariant complex tensor  $R_{\mu\nu}(\mathbf{k})$ , called the quantum geometry tensor, [52]

$$R_{\mu\nu}^\alpha(\mathbf{k}) = 2\text{Tr}[P_\alpha(\mathbf{k})\partial_\mu P_\alpha(\mathbf{k})\partial_\nu P_\alpha(\mathbf{k})] \quad (3)$$

where  $P_\alpha(\mathbf{k}) = |u_\alpha(\mathbf{k})\rangle\langle u_\alpha(\mathbf{k})|$  denotes the projection operator for the  $\alpha^{\text{th}}$ -band and  $\partial_\mu = \partial/(\partial k_\mu)$ ,  $\mu, \nu = k_x, k_y$  denote directions in momentum space. The real part of the quantum geometric tensor, denoted by  $g_{\mu\nu}^\alpha(\mathbf{k}) = \text{Re}[R_{\mu\nu}^\alpha(\mathbf{k})]$  provides a notion of a quantum distance between projected states in the Hilbert space. The imaginary part  $\text{Im}[R_{\mu\nu}^\alpha(\mathbf{k})] = \Omega_{\mu\nu}^\alpha$  is the well-known Berry curvature.

For any two-band model,  $\mathcal{H} = \sigma \cdot \mathbf{n}(\mathbf{k})$ , the quantum geometric tensor  $R_{\mu\nu}^\alpha(\mathbf{k})$  can be expressed as,

$$R_{\mu\nu}^\alpha = \frac{1}{2} \partial_\mu \hat{\mathbf{n}} \cdot \partial_\nu \hat{\mathbf{n}} + i\alpha \frac{1}{2} \hat{\mathbf{n}} \cdot \partial_\mu \hat{\mathbf{n}} \times \partial_\nu \hat{\mathbf{n}}, \quad (4)$$

where  $\alpha = \pm$  denotes the particle/hole bands, and  $\hat{\mathbf{n}} = \mathbf{n}/|\mathbf{n}|$ . The quantum metric for the massive chiral 2DEG model is valley- and spin-independent

$$g_{\mu\nu}^\pm(\mathbf{k}) = \frac{\zeta_J^2 J^2 k^{2(J-1)}}{2(\zeta_J^2 k^{2J} + m^2)^2} (m^2 \delta_{\mu\nu} + \zeta_J^2 k^{2J-2} (k^2 \delta_{\mu\nu} - k_\mu k_\nu)). \quad (5)$$

The quantum metric components satisfy  $g_{xx}(k, \varphi) = g_{yy}(k, \varphi + \pi/2)$ , implying a  $\pi/2$  rotational symmetry. The Berry curvature  $\Omega^{\eta\alpha}(\mathbf{k})$  for a chiral 2DEG is valley-dependent,

$$\Omega^{\eta\sigma}(\mathbf{k}) = -\alpha\eta \frac{\zeta_J^2 J^2}{2} \frac{mk^{2(J-1)}}{(\zeta_J^2 k^{2J} + m^2)^{3/2}}. \quad (6)$$

The Berry curvature  $\Omega(k)$  and  $Tr[g(k)]$  for biased-bilayer graphene ( $J = 2$ ) are plotted in Fig. 1 a) and

b) at different values of  $m$ . Both exhibit a mass-dependent maximum at a non-zero wavevector. The position of the maximum in  $\Omega(k)$  and  $Tr[g(k)]$  scales as  $0.84(0.86)\sqrt{m/\zeta_2}$ , respectively. This feature is important to the density and mass-dependent behavior of the geometric superfluid stiffness. Additionally, since the positive-definiteness of the quantum geometry tensor requires that the real part and imaginary part satisfy the relation  $Tr[g(\mathbf{k})] \geq |\Omega^{n\sigma}(\mathbf{k})|$ , these functions track each other.

### III. MEAN FIELD THEORY FOR SUPERCONDUCTIVITY AND EXCITON CONDENSATION

Since this paper aims to study geometric superfluid stiffness in biased-bilayer graphene, we prefer to remain agnostic of the specific pairing mechanism and, for simplicity, assume a  $k$ -independent order parameter. For the superconductor, this corresponds to an onsite sublattice independent pairing attraction. Initial experiments on superconductivity in bilayer graphene indicate an unconventional pairing mechanism, possibly resulting in a sign-changing order parameter on the Fermi surface, [48, 49, 53]. However, a  $k$ -independent order parameter on the Fermi surface has also been proposed. [54] We discuss the relevance of our findings for non-s-wave pairing toward the end.

An onsite pairing attraction results in spin-singlet Cooper pairs across the valleys  $(\mathbf{k}, \sigma, +; -\mathbf{k}, -\sigma, -)$ . The mean-field Bogoliubov-de Gennes Hamiltonian  $H_{BdG} = \sum_{\mathbf{k}} \psi_{\mathbf{k}}^\dagger \hat{H}_{BdG} \psi_{\mathbf{k}}$  in the four-component Nambu spinor basis with  $\psi_{\mathbf{k}}^\dagger = (\mathbf{c}_{\mathbf{k},\uparrow,+}^\dagger, \mathbf{c}_{-\mathbf{k},\downarrow,-}^\dagger)$ ,

$$\hat{H}_{BdG} = \begin{pmatrix} \hat{\mathcal{H}}_{0,+}(\mathbf{k}) & \Delta_{\mathbf{k}} \\ \Delta_{\mathbf{k}}^\dagger & -\hat{\mathcal{H}}_{0,-}^T(-\mathbf{k}) \end{pmatrix}. \quad (7)$$

After projection onto the electron band, the order parameter  $\Delta_{\mathbf{k}}$  is determined from the self-consistent gap equation,

$$\Delta_{\mathbf{k}} = \int \frac{d^2\mathbf{k}'}{(2\pi)^2} V_{\mathbf{k},\mathbf{k}'} \Gamma(\mathbf{k}, \mathbf{k}') \frac{\Delta_{\mathbf{k}'}}{2E_{\mathbf{k}'}} \quad (8)$$

where  $E^2(\mathbf{k}) = \xi_{\mathbf{k}}^2 + \Delta_{\mathbf{k}}^2$  with  $\xi_{\mathbf{k}} = (\epsilon_{\mathbf{k},J} - \mu)$ ,  $\mu$  denotes the Fermi energy. We assume  $\mu > 0$  (the results for  $\mu < 0$  can be attained from particle-hole symmetry of the graphene Hamiltonian).  $\Gamma(\mathbf{k}, \mathbf{k}')$ , denotes the angle-dependent chirality form factor,

$$\Gamma(\mathbf{k}, \mathbf{k}') = \frac{1}{2} (1 + \cos \theta_{\mathbf{k}} \cos \theta_{\mathbf{k}'} + \sin \theta_{\mathbf{k}} \sin \theta_{\mathbf{k}'} \cos(J\varphi_{\mathbf{k}-\mathbf{k}'})), \quad (9)$$

where  $\cos(\theta_{\mathbf{k},J}) = m/|\epsilon_{\mathbf{k},J}|$  and  $\varphi_{\mathbf{k}-\mathbf{k}'} \equiv \varphi_{\mathbf{k}} - \varphi_{\mathbf{k}'}$ . In general, the chirality form factor  $\Gamma(\mathbf{k}, \mathbf{k}')$  results in an order parameter of the form  $\Delta_{\mathbf{k}} = |\Delta_{\alpha}| e^{i\alpha\varphi_{\mathbf{k}} + i\phi}$  with chirality  $\alpha = 0, \pm 1, \pm 2, \dots$  [55] and an arbitrary global phase  $\phi = 0$ . Substituting  $\Delta_{\mathbf{k}} = |\Delta_{\alpha}| e^{i\alpha\varphi_{\mathbf{k}}}$

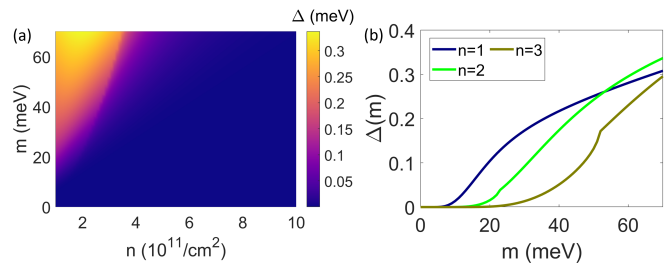


FIG. 2. The magnitude of the superconducting order parameter  $\Delta$  as a function of the mass gap and two-dimensional charge density  $n$  for bilayer graphene. Here  $V_0 = 908 \text{ meV} \cdot \text{nm}^2$  and  $\omega_c = 1 \text{ meV}$ . The unit of  $n$  is  $10^{11} \text{ cm}^{-2}$  if not specified specially.

in the gap equation above and integrating over  $\varphi_{\mathbf{k}}$  results in only three orthogonal solutions  $\alpha = 0, \pm J$  for any central interactions. For s-wave pairing interaction  $V_{\mathbf{k},\mathbf{k}'} = V_0$ , constant over thin shell over the Fermi surface  $-\omega_c < (\epsilon_{J,\mathbf{k}} - \mu) < \omega_c$ , with cutoff  $\hbar v k_c \sim 1 \text{ meV}$ , the  $\alpha = 0$  (s-wave) component provides the largest gap  $\Delta \equiv \Delta_{\alpha=0,|\mathbf{k}|=|\mathbf{k}_F|}$  for all values of  $m$ .

For weak coupling,  $\lambda = N(0)V_0/2 \ll 1$ , the superconducting gap can be expressed as  $\Delta = 2\omega_c \exp(-1/\lambda)$  when  $m = 0$ . For our calculations, we choose  $V_0 = 908 \text{ meV} \cdot \text{nm}^2$  and  $\omega_c = 1 \text{ meV}$ , which corresponds to  $\Delta \sim 0.0045 \text{ meV}$  ( $T_c \sim 30 \text{ mK}$ ) with  $m = 50 \text{ meV}$  and  $n \sim 6 \times 10^{11} \text{ cm}^{-2}$ . [48]

The order parameter exhibits exponential growth, as indicated in Fig. 2 a) and b) for  $m \sim 0 - 50 \text{ meV}$ . It then increases linearly for higher values of the mass term. This enhancement results from the large density of states at low values of  $n$ . For  $m = 0$ , the density of states in bilayer graphene is constant. Therefore,  $\Delta$  has no dependence on the Fermi energy. However, when  $m \neq 0$  at lower values of densities, there is a large density of states, resulting in an enhancement of the order parameter, as indicated in different line cuts in Fig. 2 b). The full phase diagram as a function of the mass  $m$  and the two-dimensional density  $n$  is plotted in Fig. 2 a). Next, we study the exciton gap in bilayer exciton condensates, which shows different behavior from the superconducting gap due to the long-range nature of the attractive interaction.

To realize bilayer graphene excitons condensate, we consider two bilayer graphene systems separated by a dielectric of thickness  $d$  (see Fig. 3). [50, 56–58] The Fermi energy can be tuned by the top and bottom gates to ensure electrons(holes) in the top(bottom) layers. In the particle(hole) language, the electrons in the top layer pair up with holes in the bottom layer, forming an exciton, as shown in Fig. 3. Particle-hole (PH) symmetry in exciton condensates plays the same role as time-reversal symmetry in superconductors. [59] 2D crystals generally satisfy perfect particle-hole symmetry [56, 57], therefore, they are attractive candidates to realize double-layer exciton condensates. [56, 57]

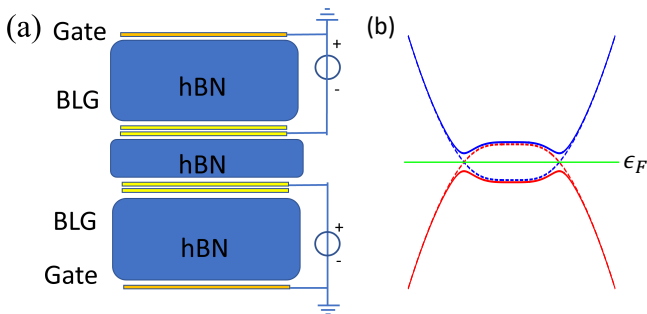


FIG. 3. (a) Schematic of dual-gated bilayer graphene device for exciton condensate. (b) The quasiparticle bands dispersion in biased bilayer graphene exciton condensate. Dashed lines indicate the non-interacting electron-hole bands. The Fermi energy is indicated in green

A similar mean field analysis can be performed for the double-biased bilayer graphene exciton condensate. The mean-field exciton parameter, here denoted by  $\Delta^\perp$ , is calculated from self-consistent similar to Eq. 8 (see the Appendix for details). For the exciton case, we take the inter-layer interaction as,  $V_D(q) = 2\pi e^2/(\epsilon q)e^{-qd}$  with the value of  $\epsilon \sim 10$  to capture the effects of screening. As in the superconducting case, the  $\alpha = 0$  solution has the largest value for the exciton gap for all values of the mass  $m$ . In the  $\alpha = 0$  pairing channel, the gap equation can be expressed as,

$$1 = \kappa \int_{-\pi/2}^{\pi/2} d\varphi \int_0^{2\cos\varphi} d\bar{q} \frac{e^{-\bar{q}k_F d} \cos\theta_{\mathbf{k}-\mathbf{q}} \cos\theta_{\mathbf{k}}}{\sqrt{\bar{\epsilon}_{\mathbf{k}-\mathbf{q}}^2 + (\bar{\Delta}^\perp)^2}} \Big|_{|\mathbf{k}|=k_F}, \quad (10)$$

where  $\kappa = e^2\gamma_1/(8\pi\epsilon(\hbar v)^2 k_F)$  is the coupling constant, all energies are measured relative to the Fermi energy  $\epsilon_F$ , and the exciton gap  $\Delta^\perp$  and chirality factors are all evaluated at  $|\mathbf{k}| = k_F$ . The  $k_F^{-1}$  dependence of the coupling constant and exponential decay as a function of  $k_F$  results from the Coulomb interaction. This results in a different dependence of the exciton gap on  $n$  and  $m$ .

The results for the exciton gap with Coulomb inter-layer interactions are plotted in Fig. 4 a) as a function of  $m$  and  $n$  for double bilayer graphene. We take the Fermi energy  $E_F \sim 3 - 35$  meV at  $m = 0$  which corresponds to the densities  $n = 0.1 - 1 \times 10^{12} \text{ cm}^{-2}$  and  $d = 1nm$ . At  $m = 0$ , the exciton gap is expected to decrease as a function of the density  $n$  (not visible due to the scale in Fig. 4 a). This is the combined effect of a weaker coupling constant  $\kappa$  value and the exponential suppression in Eq. 10.

Fig. 4 a) indicates an optimal value of  $n$  and  $m$  where the exciton gap is maximized. This behavior can be understood by studying the low and high  $n$  limits for  $m$  in Eq. 10. At low densities, electrons reside in flat-band regions with access to a large density of states, resulting in a sudden increase in the exciton gap. At large densities, the exponential term in Eq. 10 dominates, thereby

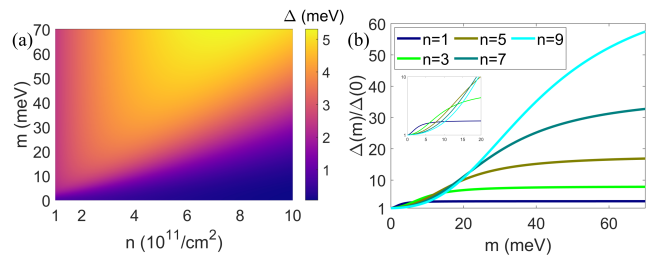


FIG. 4. The magnitude of the exciton order parameter  $\Delta$  as a function of the mass gap and two-dimensional charge density  $n$  for biased bilayer graphene. The inset in (b) shows the  $\Delta(m)$  at lower values of  $m$ .

reducing the exciton gap sharply. At intermediate values of the density  $n$ , these opposite trends conspire to produce a density-dependent local maximum value of the exciton gap. This analysis indicates an optimal value of displacement fields to search for exciton condensates in biased bilayer graphene.

The exciton gap enhancement is shown in Fig. 4 b). Even though the exciton gap is enhanced as a function of  $m$ , this enhancement is less pronounced than that of the superconducting gap; remarkably, the exciton gap also shows the opposite trend as a function of the mass and density in the enhancement. For the range of densities considered, initially, there is a larger enhancement at lower densities for masses  $m \sim 0 - 20$  meV. After this, there is a larger enhancement at higher densities past a density-dependent crossover point. These differences are due to the long-range nature of the Coulomb interaction, which results in a density-dependent coupling parameter.

#### IV. SUPERFLUID DENSITY

Our two-band superconductor is restricted to intra-band pairing between opposite spins in different valleys. In contrast, inter-band pairing results in the formation of an exciton condensate. This indicates the similarity and essential differences in the superconductors and exciton condensates. In the latter particle-hole symmetry results in the nesting of electrons and holes, while in the former time-reversal symmetry results in the nesting of electrons with opposite spins and opposite valleys. While the pairing interaction in the superconductor and exciton condensate corresponds to physically distinct processes, the mathematical structure of the mean-field Hamiltonian is similar, allowing for a unified description of the superfluid properties.

The superfluid density of the condensate characterizes its ability to carry a supercurrent. For a two-band model, taking the Fermi energy to lie within the  $\alpha^{th}$  band gives two contributions to the superfluid density for the  $\alpha^{th}$ -

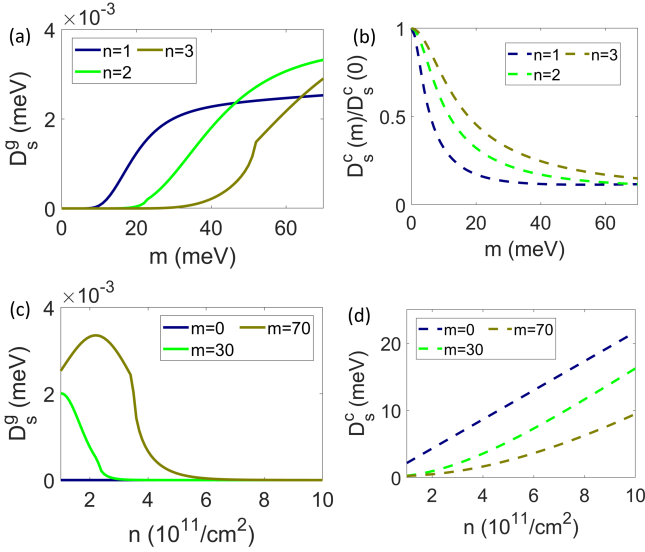


FIG. 5. The superfluid stiffness for bilayer graphene superconductor. (a) & (c) plot the geometric stiffness as a function of  $m$  for different density values  $n$  and as a function of  $n$  at different  $m$ , respectively. (b) The conventional superfluid density as a function of  $m$  for fixed  $n$  and (d) as a function of  $n$  for fixed  $m$ . The solid line labels the geometric term in all graphs, while the dashed line is the conventional superfluid density. The unit of energy is meV.

band  $D_{\mu\nu} = D_{\mu\nu}^{conv} + D_{\mu\nu}^{geo}$ , [16] where,

$$D_{\mu\nu}^{conv} = \frac{g}{L^2} \sum_{\mathbf{k}} \left( 1 - \frac{\xi_{\alpha,\mathbf{k}}}{E_{\alpha,\mathbf{k}}} \tanh\left(\frac{\beta E_{\alpha,\mathbf{k}}}{2}\right) \right) \partial_{\mu} \partial_{\nu} \epsilon_{\mathbf{k},\alpha}, \quad (11)$$

is the conventional contribution to superconductivity,

$$D_{\mu\nu}^{geo} = \frac{g}{L^2} \sum_{\mathbf{k},\alpha=\pm} \frac{2|\Delta_{\mathbf{k}}|^2 \epsilon_{\mathbf{k}}}{\alpha E_{\mathbf{k},\alpha} \mu} \tanh\left(\frac{\beta E_{\mathbf{k}}}{2}\right) g_{\mu\nu}(\mathbf{k}), \quad (12)$$

where  $E_{\mathbf{k},\alpha}^2 = \alpha^2 \xi_{\mathbf{k}}^2 + \Delta_{\mathbf{k}}^2$ , is the geometric contribution in the two-band model. At  $T = 0$ ,  $D_{\mu\nu}^{conv} = n/m^* \delta_{\mu\nu}$ , where  $m^* = \hbar^{-1}(\partial^2 \epsilon_{\mathbf{k}})/\partial k^2$ , is the effective mass. This result is independent of the symmetry of the order parameter. The  $s$ -wave order parameter maximizes the geometric superfluid stiffness, as any non  $s$ -wave symmetry reduces phase space in the integral over momentum space in Eq. 12. Therefore, our results for the  $s$ -wave symmetry provide an upper bound for the geometric superfluid density associated with the superconductor and exciton condensates in biased bilayer graphene.

Using azimuthal symmetry we can write  $D_{xy}^{geo} = 0$  and  $D_{xx}^{geo} = D_{yy}^{geo} = D^{geo}$ . For  $m = 0$ , the superfluid density can be expressed as,

$$D_s = \frac{gJ}{2\pi} \sqrt{\mu^2 + \Delta^2} + \frac{gJ\Delta^2}{2\pi\mu} \log\left(\frac{\mu + \sqrt{\Delta^2 + \mu^2}}{\mu - \sqrt{\Delta^2 + \mu^2}}\right). \quad (13)$$

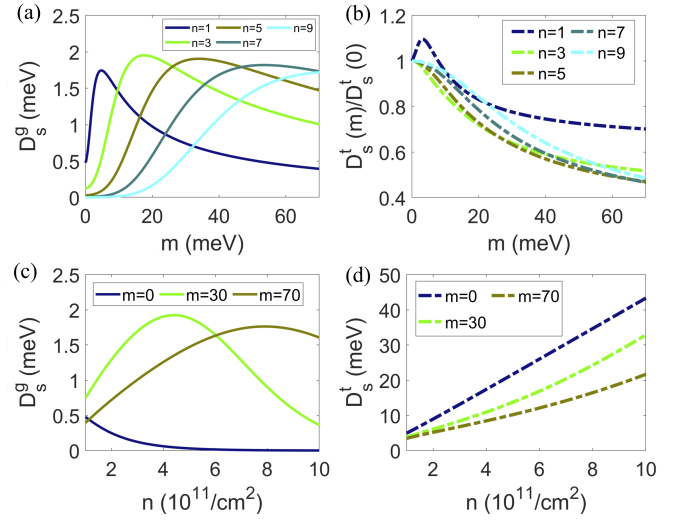


FIG. 6. The superfluid stiffness for the exciton condensate. (a) & (c) plot the geometric term as function of  $m$  for different values of density  $n$  and as a function of  $n$  at different  $m$ , respectively. (b) The ratio of the superfluid density as a function of  $m$  for fixed  $n$ . (d) Total superfluid density as a function of  $n$  for fixed  $m$ . In all graphs, the solid line labels the geometric term, while the dashed line is the total superfluid density. The unit of energy is meV.

For weak coupling,  $\mu = \epsilon_F$  and  $\Delta \ll \epsilon_F$ , resulting in a comparatively minor geometric superfluid stiffness. For  $m > 0$ , the superfluid density is calculated numerically using Eqs. 11 and 12. The geometric and conventional superfluid density as a function of  $m$  is shown in Fig. 5. As in the case  $m = 0$ , the geometric superfluid stiffness is negligible  $D_s^{geo}/D_s^{conv} \sim 10^{-4}$  for  $m \sim 50$  meV due to the small superconducting gap. The geometric superfluid stiffness is plotted as a function of  $m$  in Fig. 5 a; it follows the same behavior as the enhancement of the superconducting gap. As expected, the conventional superfluid stiffness decreases as a function of  $m$  as indicated in Fig. 5 b, due to an increase in the effective mass  $m^*$ . The decrease in the geometric superfluid stiffness in Fig. 5 (c) can be interpreted as a result of the  $\mu^{-1}$  term in Eq. 12.  $D_s^{conv}$  scales linearly with the density  $n$  for small values of the  $m$  as shown in Fig. 5 d, but exhibits an additional nonlinear suppression for larger values of  $m$ .

In contrast, the geometric superfluid stiffness for the exciton condensate exhibits much richer phenomenology as indicated in Fig. 6 a-d. Due to the large value of the exciton order parameter, the geometric superfluid stiffness has the same order as the conventional superfluid stiffness. As a result, the geometric superfluid density has a density-dependent maximum as a function of  $m$ , as seen in Fig. 6 a. However, the conventional term still determines the overall trend, except at very low densities. There is a slight enhancement in the total superfluid density at low densities  $n \lesssim 1 \times 10^{11} \text{ cm}^{-2}$  (see

Fig. 6 b). Still, the superfluid density is suppressed for higher densities as a function of  $m$ . As a result, the geometric superfluid stiffness acquires a  $n$  and  $m$  dependent maximum, as shown in Fig. 6 c). This trend follows the Berry curvature and quantum metric trace as a function of  $m$  (see Fig. 1 a & b). The exciton gap, which follows the same trend, along with the quantum metric, determines the geometric superfluid density behavior. Even though there is an approximate 20% increase in the total superfluid stiffness, it follows the same behavior as the superconductor and is primarily determined by the conventional term.

## V. BEREZINSKII-KOSTERLITZ-THOULESS TRANSITION

In superconductors and superfluids, the BKT phase transition separates the superfluid and resistive states and is associated with the binding-unbinding of vortices. [51] The critical temperature of the BKT phase transition  $T_{\text{BKT}}$  is determined from the relation  $k_B T_{\text{BKT}} = \pi D_s (\Delta(T_{\text{BKT}}), T_{\text{BKT}}) / 8$ , where  $D_s$  is the total superfluid density. A direct consequence of a geometric contribution is an increase of  $T_{\text{BKT}}$ . In the following, we only present  $T_{\text{BKT}}$  for the exciton condensate. The results for the superconductors, which exhibit negligible geometric superfluid stiffness, follow the standard relations. [51]

Fig. 7 a-f summarize our findings for  $T_{\text{BKT}}$  and critical temperatures  $T_c$  for the exciton condensate as a function of the density  $n$  and mass  $m$ . The dotted lines show  $T_{\text{BKT}}$  calculated with just the conventional term, while the  $T_{\text{BKT}}$  plotted by the solid lines taking into account the geometric contribution. As expected, adding the geometric superfluid density slightly enhances  $T_{\text{BKT}}$ . From the general trends, the enhancement is more pronounced at lower densities and higher values of  $m$ . The density and mass dependence of  $T_{\text{BKT}}$  tracks  $T_c$ , which exhibits the same qualitative behavior of the exciton gap. The enhancement in  $T_{\text{BKT}}$  at lower densities and higher masses is plotted in Figs. 7 e) & f).

## VI. DISCUSSION AND OUTLOOK

Inversion asymmetry due to a mass term  $m$  enhances the superconducting and exciton gap in biased-bilayer graphene and double bilayer-graphene. The superconducting gap is enhanced exponentially, prominent at low densities, due to the large density of state resulting from band flatness near the Dirac point. This is followed by a concomitant enhancement of the geometric superfluid stiffness. However, the conventional superfluid stiffness dominates in the weak coupling limit. The momentum independent  $s$ -wave order parameter considered in this paper provides an upper bound for the geometric superfluid density in biased-bilayer graphene. Therefore,

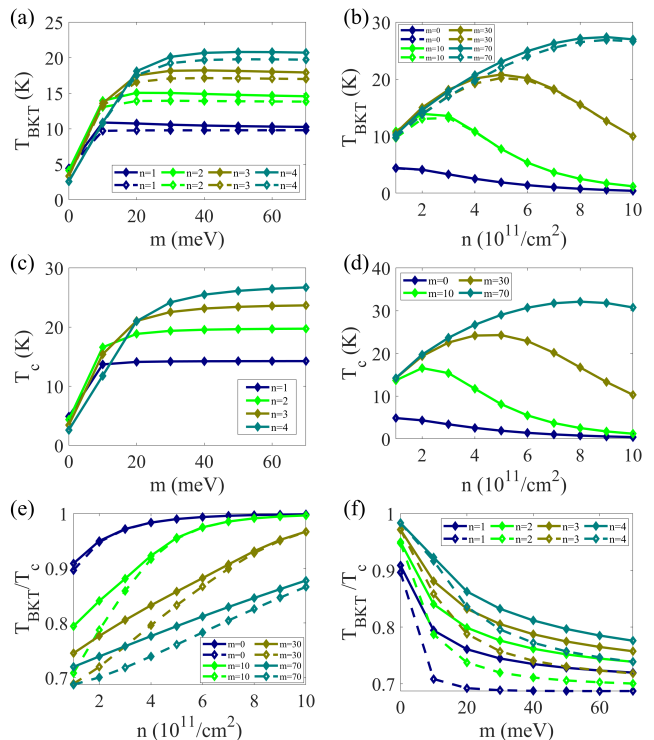


FIG. 7. The exciton condensate BKT transition temperature  $T_{\text{BKT}}$ , (a) as a function of  $m$  for different values of density  $n$  and (b) as a function of  $n$  at different  $m$ . The exciton condensate's critical temperature  $T_c$  (c) as a function of  $m$  for different  $n$  and (d) as a function of  $n$  at different  $m$ . The ratio  $T_{\text{BKT}}/T_c$ , (e) as a function of  $m$  for different  $n$  and (f) as a function of  $n$  at different  $m$ .

the geometric contribution to superfluidity in bilayer graphene superconductors should be negligible. [48] This is not so for the exciton condensate.

For the exciton condensate, the band structure modification due to the mass term and the long-range nature of the Coulomb interactions produces a modest increase in the exciton gap. Coincidentally, the exciton gap is maximized for an optimal value of the density-dependent mass  $m(n)$  with critical temperatures  $T_c \sim 1 - 10K$ . These critical temperature estimates are consistent with more sophisticated studies of exciton condensation in transition-metal dichalcogenides [60], implying mean-field theory qualitatively captures the behavior of the exciton condensate gap in biased bilayer graphene. These larger values of the exciton condensate gap result in a comparable geometric superfluid density compared to the conventional contribution. This geometric contribution is more pronounced at lower densities and higher mass values, where flatter regions of the electronic band dispersion influence the exciton condensate. An experimental consequence of the more significant total superfluid density is an increase in the BKT transition temperatures of the exciton condensate in biased bilayer graphene.

## ACKNOWLEDGMENTS

The authors acknowledge helpful discussions with G. Jiang and Han Fu. Y.B. was supported by the University of Nevada, Reno VPRI startup grant PG19012. E.R. acknowledges support from DOE, grant No. DE-SC0022245. We acknowledge William & Mary Research Computing for providing computational resources and/or technical support that have contributed to the results reported within this paper. URL: <https://www.wm.edu/it/rc>. X.U. acknowledges funding from the National Natural Science Foundation of China (Grant No. 11904143), the Natural Science Foundation of Guangxi Province Grant No. 2020GXNSFAA297083, GuiKe AD20297045.

## VII. APPENDIX: MEAN FIELD THEORY FOR THE EXCITON CONDENSATE

Since indirect excitons in spatially separated electron-hole bilayer are protected from recombination [61], these systems are ideal platforms for exciton (electron-hole bound pair) condensation. [62] Particle-hole (PH) symmetry in exciton condensates plays the same role as time-reversal symmetry in superconductors. [59] 2D crystals generally satisfy perfect particle-hole symmetry [56, 57] and are attractive candidates to realize double-layer exciton condensates. [56, 57]. The size of the superfluid exciton gap in graphene double-layer condensate has been predicted to be  $1mK - 100K$ . [50, 56, 57, 63–65] The wide range of transition temperatures predicted depend on the level of the approximation in treatment of screening effects, which are of the order of the Fermi wavevector and can reduce the exciton gap. [50, 63–65] Similar double-layer exciton condensates can be engineered in bilayer graphene and hybrid systems. To realize a bilayer exciton condensate, we propose the experimental setup in the figure, where the two chiral 2DEGs are separated by a dielectric of thickness  $d$ , and top and bottom gates. The device's geometry is like Fig. 3 (a). For the single-layer graphene, the hBN substrate provides a staggering potential, which breaks the sublattice symmetry and creates an effective mass for the electrons. Additionally, for the bilayer graphene systems, the effective mass corresponds to the electric field potential difference within each bilayer.

In both cases, the densities of electrons and holes in the upper or lower graphene (bilayer graphene) can be tuned by an electric field applied perpendicular to the combined hetero-structure, as indicated in the schematic figure. The layers are gated separately with the gate potential ( $V_g, -V_g$ ) in the top and bottom layers. The gate potential is adjusted for a p-type Fermi surface (FS) in one layer nested with the n-type FS in the other layer. The setup in the figure allows independent control of the doping and layer potential. From now, without loss of generality, we assume that the gate voltages are such that the Fermi energy lies in the conduction band for

the top-layer ( $\sigma = 1(+)$ ) and in the valence band for the bottom-layer ( $\sigma = 2(-)$ ). The single particle energy dispersion of the low energy bands of hetero-structure is symmetric about the Fermi energy due to particle-hole symmetry with  $\zeta_{\mathbf{k},J,+} = -V_g + \varepsilon_{\mathbf{k},J}$  and  $\zeta_{\mathbf{k},J,-} = V_g - \varepsilon_{\mathbf{k},J}$  as indicated in Fig. 3 (b).

Assuming that the exciton order parameter  $\Delta$  is smaller than the applied gate potential  $|V_g|$ , the density-density interactions can be projected on the electron band in the top layer and the hole band in the bottom layer. The interaction Hamiltonian can be expressed as,

$$\mathcal{H}_{int} = \frac{1}{2L^2} \sum_{q,\alpha=\pm} (V_{\mathbf{q}} \bar{\rho}_{\mathbf{q},\alpha} \bar{\rho}_{-\mathbf{q},\alpha} + V_{\mathbf{q}}^d \bar{\rho}_{\mathbf{q},\alpha} \bar{\rho}_{-\mathbf{q},-\alpha}), \quad (14)$$

where  $L^2$  denotes the area of the heterostructure,  $\sigma = \pm = (t, b)$  are identified with the electron bands in the top layer and the hole bands in the bottom layer,  $V_{\mathbf{q}}^d$  ( $V_{\mathbf{q}}$ ) refers to the interlayer (intralayer) interaction, and the projected density operator can be expressed as,

$$\bar{\rho}_{\mathbf{q},\alpha} = \sum_{\mathbf{k},\alpha} \langle \chi_{J,\alpha}(\mathbf{k} + \mathbf{q}) | \chi_{J,\alpha}(\mathbf{k}) \rangle \gamma_{\mathbf{k}+\mathbf{q},\alpha,\sigma}^\dagger \gamma_{\mathbf{k},\alpha,\sigma}, \quad (15)$$

where  $\gamma_{\mathbf{k},\sigma}^\dagger$  ( $\gamma_{\mathbf{k},\sigma}$ ) denotes the  $\alpha^{th}$  band creation and annihilation operator at  $\mathbf{k}$ , and  $\sigma$  denotes the spin and valley degrees of freedom, which remain unaffected by the mass term  $m$ . The form factors associated with the wavefunction overlap in the projected density determine the symmetry of the exciton order parameter  $\Delta$  and the fluctuations of the exciton condensate, as we show next.

For a non-zero expectation value for the exciton order parameter one obtains a mean-field Hamiltonian,  $\mathcal{H}_{MF} = -\sum_{\mathbf{k},\sigma,\sigma'} \gamma_{\mathbf{k},\sigma}^\dagger \mathbf{\Delta}_{\mathbf{k}} \cdot \boldsymbol{\tau}_{\sigma\sigma'} \gamma_{\mathbf{k},\sigma'}$ , where  $\mathbf{\Delta} = (\Delta^x, \Delta^y, \Delta^z)$  denote the mean-fields and  $\boldsymbol{\tau} = (\tau^x, \tau^y, \tau^z)$  are the  $2 \times 2$  Pauli matrices acting in the layer pseudospin space. The transverse components of the pseudospin field  $\mathbf{\Delta}_{\mathbf{k}}$  define a complex order parameter  $\Delta_{\mathbf{k}}^\perp = \Delta_{\mathbf{k}}^x - i\Delta_{\mathbf{k}}^y$ , whose magnitude  $|\Delta_{\mathbf{k}}^\perp|$  determines the strength of the particle-hole condensate. The mean-fields  $\mathbf{\Delta}_{\mathbf{k}}$  are given by the following self-consistent equations:

$$\begin{aligned} \Delta_{\mathbf{k}}^z &= \eta_{\mathbf{k}} + \frac{1}{2L^2} \sum_{\mathbf{p}} [V_{\mathbf{k}-\mathbf{p}} \Gamma(\mathbf{k}, \mathbf{p}) - E_H] \left[ 1 + \frac{\Delta_{\mathbf{p}}^z}{E_{\mathbf{p}}} f\left(\frac{E_{\mathbf{p}}}{2}\right) \right]; \\ \Delta_{\mathbf{k}}^\perp &= \frac{1}{2L^2} \sum_{\mathbf{p}} V_{\mathbf{k}-\mathbf{p}}^d \Gamma(\mathbf{k}, \mathbf{p}) \frac{\Delta_{\mathbf{p}}^\perp}{E_{\mathbf{p}}} f\left(\frac{E_{\mathbf{p}}}{2}\right), \end{aligned} \quad (16)$$

where  $\eta_{\mathbf{k}} = |\zeta_{\mathbf{k},J}|$ ,  $f(x) = \tanh(\beta x)$  and  $\beta = 1/(k_B T)$  denotes the inverse thermal energy. The interlayer Coulomb interaction in the direct channel,  $E_H = 2\pi e^2/\epsilon g d$  capture the layer charging energy,  $g = 4$  is the total spin and valley degeneracy and  $\epsilon$  the dielectric constant of the embedding media. The bands in the presence of the exciton order parameter  $\Delta_{\mathbf{k}}^\perp$  are given as  $E_{\mathbf{k}} = \sqrt{(\Delta_{\mathbf{k}}^z)^2 + |\Delta_{\mathbf{k}}^\perp|^2}$ .

### VIII. APPENDIX: SUPERFLUID DENSITY: GEOMETRIC AND CONVENTIONAL CONTRIBUTION

The Kubo formula for the superfluid density [16] can be expressed as,

$$D_{\mu\nu} = \frac{g}{L^2} \sum_{\mathbf{k}, ij} \frac{n(E_j) - n(E_i)}{E_i - E_j} \left( \langle \psi_i | \partial_\mu H | \psi_j \rangle \langle \psi_j | \partial_\nu H | \psi_i \rangle - \langle \psi_i | \partial_\mu H \gamma_z | \psi_j \rangle \langle \psi_j | \gamma_z \partial_\nu H | \psi_i \rangle \right), \quad (17)$$

where  $g = 2(4)$  denotes the degeneracy of the superconductor (exciton condensate),  $i(j) = (\pm, \alpha)$  label the particle-hole Bogoliubov-deGennes (BdG) bands in the  $\alpha = \pm$  band, with  $\psi_i$  and  $E_i$  denoting the respective BdG eigenfunctions and eigenvalues, and  $n(E)$  corresponds to the Fermi-Dirac distribution. The first term corresponds to the diamagnetic contribution, while the second term is the paramagnetic contribution. At points of degeneracy for a gapless order parameter difference between the Fermi function is replaced by their derivative with respect to the energy.

The gauge field in superconductor and exciton condensate corresponds to physically distinct processes, namely the magnetic field for superconductors and displacement field asymmetry  $\mathbf{q} = e(\vec{A}_t - \vec{A}_b)$  (where  $\vec{A}_i$  denotes the electromagnetic gauge field in the  $i^{\text{th}}$ -layer) for the latter. Nevertheless, the mathematical structure of the BdG mean-field Hamiltonian is the same, allowing for a unified description. In the case of the superconductor, we assume the  $\mu > 0$ . The superconducting BdG eigenstates for the  $\alpha = +$  band can be expressed in the basis set  $(\mathbf{k}, \uparrow, +; -\mathbf{k}, \downarrow, -)$ , are  $\psi_{\alpha,-}^\dagger(\mathbf{k}) = (u_\alpha, v_\alpha)$  and  $\psi_{\alpha,-}^\dagger(\mathbf{k}) = (-v_\alpha, u_\alpha)$  with

$$u_\alpha^2(\mathbf{k}) = \frac{1}{2} \left( 1 + \frac{\xi_\alpha}{E_\alpha} \right) \quad v_\alpha^2(\mathbf{k}) = \frac{1}{2} \left( 1 - \frac{\xi_\alpha}{E_\alpha} \right) \quad (18)$$

where  $\xi_\alpha = \epsilon_\alpha(\mathbf{k}) - \mu$  and  $E_\alpha = \sqrt{\xi_\alpha^2 + \Delta^2}$ . The BdG eigenstates for exciton condensate can be represented by the same expression with a different basis choice  $(\mathbf{k}, \sigma, e; -\mathbf{k}, \sigma, h)$ . This is due to the unified description allowed by the superconductor and exciton condensate.

For a  $\mathbf{k}$ -dependent and real order parameter  $\Delta_{\mathbf{k}}$ , we can express the matrix element in the above expression as

$$\langle \psi_{\alpha',+} | \partial_\mu H | \psi_{\alpha,-} \rangle = -(v_{\alpha,\mathbf{k}} u_{\alpha,\mathbf{k}} + u_{\alpha',\mathbf{k}} v_{\alpha,\mathbf{k}}) \langle u_{\alpha'} | \partial_\mu H | u_\alpha \rangle, \quad (19)$$

where  $u_\alpha$  is the Bloch wavefunction of the band. The matrix element above is calculated as usual

$$\langle u_{\alpha'} | \partial_\mu H | u_\alpha \rangle = \partial_\mu \epsilon_\alpha \delta_{\alpha\alpha'} + (\epsilon_{\alpha'}(\mathbf{k}) - \epsilon_\alpha(\mathbf{k})) \langle \partial_\mu u_\alpha | u_{\alpha'} \rangle. \quad (20)$$

Taking the Fermi energy to lie within the  $\alpha^{\text{th}}$  band, a straightforward calculation [16] gives two contributions to the superfluid density for the  $\alpha^{\text{th}}$ -band  $D_{\mu\nu} = D_{\mu\nu}^{\text{conv}} + D_{\mu\nu}^{\text{geo}}$ , where,

$$D_{\mu\nu}^{\text{conv}} = \frac{g}{L^2} \sum_{\mathbf{k}} \left( 1 - \frac{\xi_{\alpha,\mathbf{k}}}{E_{\alpha,\mathbf{k}}} \partial_\mu \partial_\nu \epsilon_{\alpha,\mathbf{k}} \right), \quad (21)$$

is the conventional contribution to superconductivity, while the geometric contribution  $D_{\mu\nu}^{\text{geo}}$  becomes,

$$D_{\mu\nu}^{\text{geo}} = \frac{g}{L^2} \sum_{\mathbf{k}} |\Delta_{\mathbf{k}}|^2 \sum_{\alpha \neq \alpha'} \frac{(\xi_\alpha - \xi_{\alpha'})}{\xi_{\alpha'} + \xi_\alpha} \left( \frac{1}{E_{\alpha'}} - \frac{1}{E_\alpha} \right) \left[ \langle \partial_\mu u_\alpha | u_{\alpha'} \rangle \langle u_{\alpha'} | \partial_\nu u_\alpha \rangle + h.c. \right], \quad (22)$$

where  $\alpha = \pm$  corresponds to the particle/hole bands of the chiral 2DEG. For the two-band model, the geometric superfluid can be expressed as

$$D_{\mu\nu}^{\text{geo}} = \frac{g}{L^2} \sum_{\mathbf{k}, \alpha=\pm} 2|\Delta_{\mathbf{k}}|^2 \alpha \frac{\epsilon_{\alpha,\mathbf{k}}}{\mu E_{\mathbf{k}}} g_{\mu\nu}(\mathbf{k}). \quad (23)$$

- 
- [1] Y. Cao, V. Fatemi, A. Demir, S. Fang, S. L. Tomarken, J. Y. Luo, J. D. Sanchez-Yamagishi, K. Watanabe, T. Taniguchi, E. Kaxiras, *et al.*, *Nature* **556**, 80 (2018).
- [2] M. Yankowitz, S. Chen, H. Polshyn, Y. Zhang, K. Watanabe, T. Taniguchi, D. Graf, A. F. Young, and C. R. Dean, *Science* **363**, 1059 (2019).
- [3] Y. Cao, V. Fatemi, S. Fang, K. Watanabe, T. Taniguchi, E. Kaxiras, and P. Jarillo-Herrero, *Nature* **556**, 43 (2018).
- [4] X. Lu, P. Stepanov, W. Yang, M. Xie, M. A. Aamir, I. Das, C. Urgell, K. Watanabe, T. Taniguchi, G. Zhang, *et al.*, *Nature* **574**, 653 (2019).
- [5] G. Chen, A. L. Sharpe, P. Gallagher, I. T. Rosen, E. J. Fox, L. Jiang, B. Lyu, H. Li, K. Watanabe, T. Taniguchi, *et al.*, *Nature* **572**, 215 (2019).
- [6] J. M. Park, Y. Cao, K. Watanabe, T. Taniguchi, and P. Jarillo-Herrero, *Nature* **590**, 249 (2021).
- [7] Y. Cao, J. M. Park, K. Watanabe, T. Taniguchi, and P. Jarillo-Herrero, *Nature* **595**, 526 (2021).
- [8] A. L. Sharpe, E. J. Fox, A. W. Barnard, J. Finney, K. Watanabe, T. Taniguchi, M. A. Kastner, and D. Goldhaber-Gordon, *Science* **365**, 605 (2019).
- [9] G. W. Burg, J. Zhu, T. Taniguchi, K. Watanabe, A. H. MacDonald, and E. Tutuc, *Phys. Rev. Lett.* **123**, 197702 (2019).
- [10] Y. Cao, D. Rodan-Legrain, O. Rubies-Bigorda, J. M. Park, K. Watanabe, T. Taniguchi, and P. Jarillo-Herrero, *Nature* **583**, 215 (2020).
- [11] H. Polshyn, J. Zhu, M. A. Kumar, Y. Zhang, F. Yang, C. L. Tschirhart, M. Serlin, K. Watanabe, T. Taniguchi, A. H. MacDonald, and A. F. Young, *Nature* **588**, 66 (2020).
- [12] S. Chen, M. He, Y.-H. Zhang, V. Hsieh, Z. Fei, K. Watanabe, T. Taniguchi, D. H. Cobden, X. Xu, C. R. Dean,



- and M. Yankowitz, *Nature Physics* **17**, 374 (2021).
- [13] Y. Xie, A. T. Pierce, J. M. Park, D. E. Parker, E. Khalaf, P. Ledwith, Y. Cao, S. H. Lee, S. Chen, P. R. Forrester, K. Watanabe, T. Taniguchi, A. Vishwanath, P. Jarillo-Herrero, and A. Yacoby, *Nature* **600**, 439 (2021).
- [14] R. Bistritzer and A. H. MacDonald, *Proceedings of the National Academy of Sciences* **108**, 12233 (2011).
- [15] S. Peotta and P. Törmä, *Nature Communications* **6**, 8944 (2015).
- [16] L. Liang, T. I. Vanhala, S. Peotta, T. Siro, A. Harju, and P. Törmä, *Phys. Rev. B* **95**, 024515 (2017).
- [17] X. Hu, T. Hyart, D. I. Pikulin, and E. Rossi, *Phys. Rev. Lett.* **123**, 237002 (2019).
- [18] F. Xie, Z. Song, B. Lian, and B. A. Bernevig, *Phys. Rev. Lett.* **124**, 167002 (2020).
- [19] A. Julku, T. J. Peltonen, L. Liang, T. T. Heikkilä, and P. Törmä, *Phys. Rev. B* **101**, 060505 (2020).
- [20] A. Julku, G. M. Bruun, and P. Törmä, *Physical review letters* **127**, 170404 (2021).
- [21] P. Törmä, L. Liang, and S. Peotta, *Physical Review B* **98**, 220511 (2018).
- [22] Z. Wang, G. Chaudhary, Q. Chen, and K. Levin, *Physical Review B* **102**, 184504 (2020).
- [23] A. Julku, S. Peotta, T. I. Vanhala, D.-H. Kim, and P. Törmä, *Physical review letters* **117**, 045303 (2016).
- [24] E. Rossi, *Current Opinion in Solid State and Materials Science* **25**, 100952 (2021).
- [25] S. A. Parameswaran, R. Roy, and S. L. Sondhi, *Comptes Rendus Physique* **14**, 816 (2013), topological insulators / Isolants topologiques.
- [26] R. Roy, *Phys. Rev. B* **90**, 165139 (2014).
- [27] F. D. M. Haldane, *Phys. Rev. Lett.* **107**, 116801 (2011).
- [28] S. A. Parameswaran, R. Roy, and S. L. Sondhi, *Phys. Rev. B* **85**, 241308 (2012).
- [29] N. Regnault and B. A. Bernevig, *Phys. Rev. X* **1**, 021014 (2011).
- [30] T. S. Jackson, G. Möller, and R. Roy, *Nature Communications* **6**, 8629 (2015).
- [31] B. Andrews and A. Soluyanov, *Phys. Rev. B* **101**, 235312 (2020).
- [32] C. Repellin and T. Senthil, *Phys. Rev. Res.* **2**, 023238 (2020).
- [33] P. J. Ledwith, G. Tarnopolsky, E. Khalaf, and A. Vishwanath, *Phys. Rev. Res.* **2**, 023237 (2020).
- [34] P. Wilhelm, T. C. Lang, and A. M. Läuchli, *Phys. Rev. B* **103**, 125406 (2021).
- [35] X. Hu, T. Hyart, D. I. Pikulin, and E. Rossi, *Physical Review B* **105**, L140506 (2022).
- [36] J. Schrieffer, *Theory Of Superconductivity*, Advanced Books Classics (Avalon Publishing, 1999).
- [37] Z. Wang, D. A. Rhodes, K. Watanabe, T. Taniguchi, J. C. Hone, J. Shan, and K. F. Mak, *Nature* **574**, 76 (2019).
- [38] J. Herzog-Arbeitman, V. Peri, F. Schindler, S. D. Huber, and B. A. Bernevig, *Physical review letters* **128**, 087002 (2022).
- [39] M. Tovmasyan, S. Peotta, P. Törmä, and S. D. Huber, *Physical Review B* **94**, 245149 (2016).
- [40] J. S. Hofmann, E. Berg, and D. Chowdhury, *Physical Review B* **102**, 201112 (2020).
- [41] H. Tian, X. Gao, Y. Zhang, S. Che, T. Xu, P. Cheung, K. Watanabe, T. Taniguchi, M. Randeria, F. Zhang, C. N. Lau, and M. W. Bockrath, *Nature* **614**, 440 (2023).
- [42] E. McCann and V. I. Fal'ko, *Phys. Rev. Lett.* **96**, 086805 (2006).
- [43] H. Min and A. H. MacDonald, *Phys. Rev. B* **77**, 155416 (2008).
- [44] F. Guinea, A. H. Castro Neto, and N. M. R. Peres, *Phys. Rev. B* **73**, 245426 (2006).
- [45] M. Koshino and E. McCann, *Phys. Rev. B* **81**, 115315 (2010).
- [46] M. Serbyn and D. A. Abanin, *Phys. Rev. B* **87**, 115422 (2013).
- [47] M. Koshino and E. McCann, *Phys. Rev. B* **83**, 165443 (2011).
- [48] H. Zhou, L. Holleis, Y. Saito, L. Cohen, W. Huynh, C. L. Patterson, F. Yang, T. Taniguchi, K. Watanabe, and A. F. Young, *Science* **375**, 774 (2022).
- [49] Y. Zhang, R. Polski, A. Thomson, A. Lantagne-Hurtubise, C. Lewandowski, H. Zhou, K. Watanabe, T. Taniguchi, J. Alicea, and S. Nadj-Perge, *Nature* **613**, 268 (2023).
- [50] A. Perali, D. Neilson, and A. R. Hamilton, *Phys. Rev. Lett.* **110**, 146803 (2013).
- [51] J. M. Kosterlitz and D. J. Thouless, *Journal of Physics C: Solid State Physics* **6**, 1181 (1973).
- [52] J. Provost and G. Vallee, *Communications in Mathematical Physics* **76**, 289 (1980).
- [53] Y.-Z. Chou, F. Wu, J. D. Sau, and S. Das Sarma, *Phys. Rev. B* **105**, L100503 (2022).
- [54] Z. Dong, A. V. Chubukov, and L. Levitov, "Spin-triplet superconductivity at the onset of isospin order in biased bilayer graphene," (2022), [arXiv:2205.13353 \[cond-mat.supr-con\]](https://arxiv.org/abs/2205.13353).
- [55] J. Zhang and E. Rossi, *Phys. Rev. Lett.* **111**, 086804 (2013).
- [56] H. Min, R. Bistritzer, J.-J. Su, and A. H. MacDonald, *Phys. Rev. B* **78**, 121401 (2008).
- [57] C.-H. Zhang and Y. N. Joglekar, *Phys. Rev. B* **77**, 233405 (2008).
- [58] R. M. Lutchyn, E. Rossi, and S. Das Sarma, *Physical Review A* **82**, 061604 (2010).
- [59] R. Bistritzer and A. H. MacDonald, *Phys. Rev. Lett.* **101**, 256406 (2008).
- [60] B. Debnath, Y. Barlas, D. Wickramaratne, M. R. Neupane, and R. K. Lake, *Phys. Rev. B* **96**, 174504 (2017).
- [61] J. P. Eisenstein and A. H. MacDonald, *Nature* **432**, 691 (2004).
- [62] J. M. Blatt, K. W. Böer, and W. Brandt, *Phys. Rev.* **126**, 1691 (1962).
- [63] M. Y. Kharitonov and K. B. Efetov, *Phys. Rev. B* **78**, 241401 (2008).
- [64] D. S. L. Abergel, M. Rodriguez-Vega, E. Rossi, and S. Das Sarma, *Phys. Rev. B* **88**, 235402 (2013).
- [65] I. Sodemann, D. A. Pesin, and A. H. MacDonald, *Phys. Rev. B* **85**, 195136 (2012).